Institute for Advanced Simulation

First-Principles Based Multiscale Modelling of Alloys

Stefan Müller

published in

Multiscale Simulation Methods in Molecular Sciences,
J. Grotendorst, N. Attig, S. Blügel, D. Marx (Eds.),
Institute for Advanced Simulation, Forschungszentrum Jülich,
NIC Series, Vol. **42**, ISBN 978-3-9810843-8-2, pp. 291-320, 2009.

http://www.fz-juelich.de/nic-series/volume42

First-Principles Based Multiscale Modelling of Alloys

Stefan Müller[1,2]

[1] Lehrstuhl für Theoretische Physik 2
Universität Erlangen-Nürnberg
Staudtstrasse 7, 91058 Erlangen, Germany

[2] Lehrstuhl für Festkörperphysik
Universität Erlangen-Nürnberg
Staudtstrasse 7, 91058 Erlangen, Germany
E-mail: stefan.mueller@physik.uni-erlangen.de

Although modern computer codes based on density functional theory (DFT) allow the reliable prediction of many surface and bulk properties of solids, they cannot be applied, when the problem of interest demands a consideration of huge configuration spaces or model systems containing many thousand atoms. Important examples are precipitation and segregation in metal alloys where substitutional ordering phenomena on a mesoscopic scale are involved. Moreover, in general first-principles methods based on DFT do not allow for exchange processes between atoms and therefore, do not consider configurational enthalpies being a prerequisite for modelling the temperature-dependence of decomposition reactions or segregation phenomena. In this contribution, recent developments, possibilities and limitations to study ordering phenomena and ground-state properties based on first-principles methods will be discussed. It will be demonstrated how the combination of DFT calculations with so-called Cluster Expansions and Monte-Carlo simulations allows for a quantitative prediction of alloy properties from the miscroscopic up to the meso-, and even macroscale without any empirical parameters.

1 Introduction: The Definition of "Order"

If A- and B-atoms are forced to crystallize on a common lattice, they may either order (AB-bonds) or cluster (AA- and BB-bonds) depending on whether the occupation of neighboring lattice sites by identical or different species is energetically favoured. However, the situation becomes more complex, when temperature comes into play: The temperature-composition phase diagram of a binary solid state alloy, $\mathrm{A}_{1-x}\mathrm{B}_x$, may consist of homogeneous single-phase regions (such as ordered compounds A_mB_n) as well as heterogeneous, phase-coexistence regions[1]. Besides intermetallic compounds, i.e. long-range ordered (LRO) phases, which are mostly observed at low temperatures, in many binary metal systems so-called "solid solutions" exist. Although such solid solutions are often described by a lattice grid randomly occupied by A and B atoms, more or less *all* solid solutions show substitutional short-range order (SRO). Indeed, SRO may have a tremendous influence on the energy and stability of this alloy phase. Consequently, the physical properties of solid solutions must be modelled by a *disordered* alloy which is not necessarily a *random* alloy. In fact, SRO makes a quantitative, theoretical description of alloys on a quantum-mechanical basis rather complex. One may ask, if it is really necessary to consider SRO for a quantitative description of an alloy's stability. Fo this, we consider the solid solution of α-brass (Cu-rich Cu-Zn). For this phase, it well-known from experiment[2] and theory[3] that characteristic SRO occurs. This can be seen in Figure (1) which compares calculated mixing enthalpies[3], $\Delta H_{mix}(x,T)$, for different temperatures with experimental data

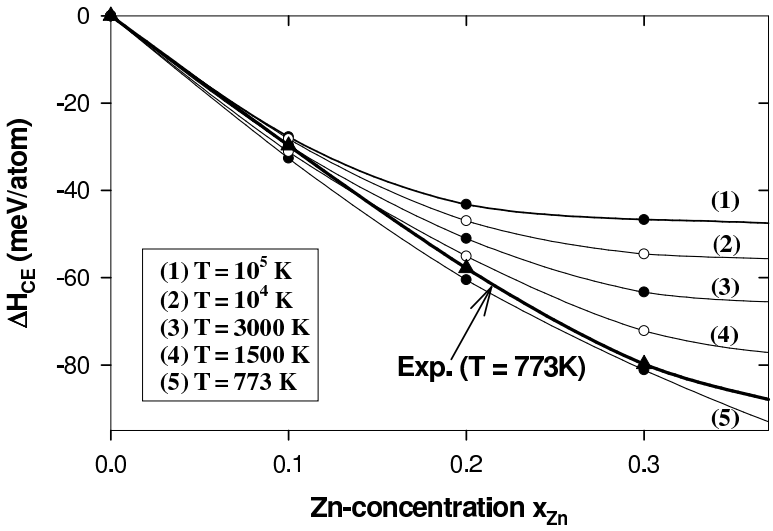

Figure 1. Calculated mixing enthalpies of α-brass for different temperatures[3], in comparison with experimental data[4] (bold line).

taken from Hultgren's book[4]. The mixing enthalpy, ΔH_f^{DFT} per atom of configuration σ is defined as

$$\Delta H_{mix}(\sigma) = \frac{1}{N} E^{tot}(A_{1-x}B_x, \sigma) - x E_A^{tot}(a_A) - (1-x) E_B^{tot}(a_B) \qquad (1)$$

with N being the total number of atoms in the disordered alloy. $E^{tot}(A_{1-x}B_x, \sigma)$ is the total energy of the geometrically fully relaxed configuration σ with concentration x of B-atoms ($0 \leq x \leq 1$). Furthermore, a_A and a_B are the equilibrium lattice constants of the elements A and B, $E_A^{tot}(a_A)$ and $E_B^{tot}(a_B)$ are the respective total energies. Since all total energy values are negative, a positive sign of ΔH_{mix} stands for phase-separation, while a negative sign of ΔH_{mix} stands for ordering (as in the case of α-brass). The theoretical calculations in Figure (1) are performed by combining density functional theory with methods from statistical physics which will be explained in the next section: We start with the random alloy ($T \to \infty$) and go down to temperatures where short-range order sets in. Figure 1 shows that the calculation neglecting ordering phenomena ($T = 10^5$K, corresponding to a random alloy) leads to much higher mixing enthalpies than in experiment. For higher Zn concentrations a good agreement between experiment and calculated mixing enthalpies can only be reached, if ordering phenomena are taken into account.

Before we discuss, how to calculate SRO, we need a a measure *how* to quantify it. Ziman[5] nicely described the difficulty to handle ordered zones in a disordered matrix by Fig. (2): For the given configuration, we cannot decide, if the atom marked by an arrow belongs to a "cluster of pure A-atoms" or to a "region of perfect AB-order". He demonstrated by applying percolation theory that almost every A-atom belongs to an infinite cluster of A atoms. Paradoxically, if we are looking for ordered domains (Fig. (2)), then almost every atom belongs to an infinite domain with perfect AB-ordering. Help comes by introducing statistical concepts[5–7]: For a system consisting of N sites each surrounded by M neigh-

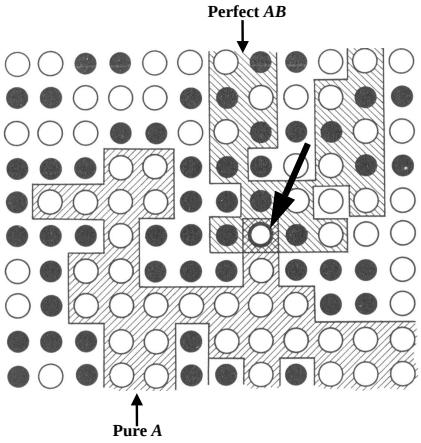

Figure 2. The dilemma in describing ordering (taken from Ziman[5]): Does the atom marked by an arrow belong to "a cluster of pure A-atoms", or to a "region of perfect AB-order"?

bors, the probability of a bond being of AB-type is given by

$$P_{AB} = lim_{N\to\infty}\left(\frac{N_{AB}}{\frac{1}{2}MN}\right) \tag{2}$$

with N_{AB} being the total number of AB-type bonds. The denominator gives the total number of bonds in the system. If we assume that each site of the system is independently occupied by an A- or B-atom with probability x_A or x_B ($x_A + x_B = 1$), then P_{AB} would be $2x_Ax_B$. Then, the nearest-neighbor correlation parameter Γ_{AB} can be defined as

$$\Gamma_{AB} = \frac{1}{2}P_{AB} - x_Ax_B.$$

Dividing Γ_{AB} by $-x_Ax_B$ leads to the well-known *Warren-Cowley short-range order parameter*[8]

$$\alpha_j = 1 - \frac{P^j_{AB}}{2x_Ax_B}. \tag{3}$$

Here, α_j is already extended to arbitrary neighbor distances j. The sign of α_j indicates whether atoms in a given distance j prefer AB-ordering ($\alpha_j < 0$) or clustering ($\alpha_j > 0$). The SRO parameter are normalized such that $-1 \leq \alpha_j \leq +1$. Since α_j can be determined from diffuse X-ray and neutron diffraction experiments[9–11], a *quantitative* comparison between calculation and measurement is possible.

If we wish to describe and understand the properties of different solid phases and their stability on a quantum-mechanical basis, we have to solve three fundamental problems (Fig. 3):

(i) *The configurations-space problem:* In general, first-principles calculations only considers atomic relaxations in the unit cell, but do not allow for exchange processes between

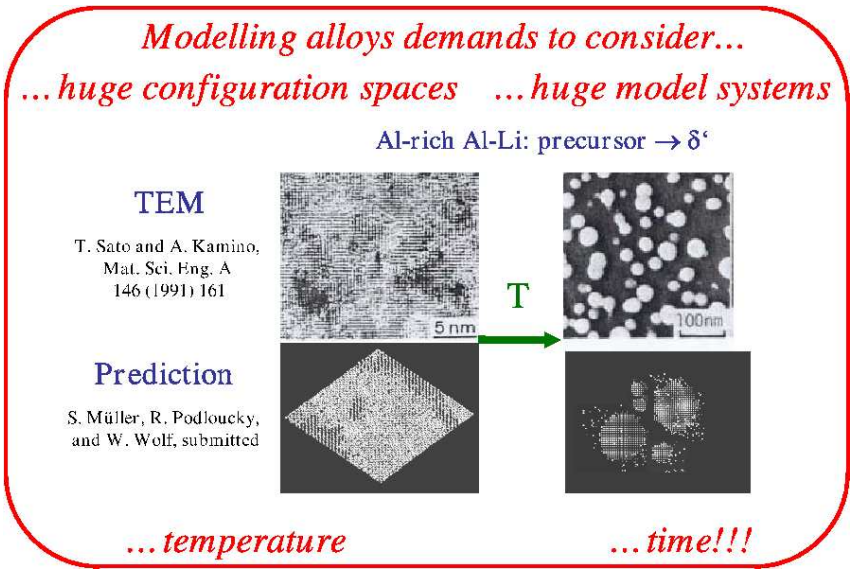

Figure 3. Comparison between predicted and measured precipitation in Al-rich Al-Li alloys. The theoretical description demands to overcome the four fundamental problems in materials modelling.

individual atoms. The latter is a prerequisite for an efficient and reliable ground-state search, i.e. for finding the configuration being lowest in energy for a given concentration.
(ii) *The multiscale problem:* The quantitative prediction of short-range order phenomena often requires models with giant unit cells. Model systems containing up to 10^6 atoms may be demanded, i.e. much more than the about 500 metal atoms treatable by today's computers.
(iii) *The temperature problem:* The temperature-dependence of ordering phenomena must not be neglected. However, in general, electronic structure theories are constructed to study $T = 0$K properties.

In principle, there is a fourth problem, namely the fact that many properties of alloys are not understandable in the framework of thermodynamics. In order to go beyond equilibrium properties of the system, kinetic approaches have to be considered. As a consequence the system's properties become *time-dependent*. As will be demonstrated in section 2, it is not an easy task to transform kinetic simulation results into a real-time scale.

The main aim of this lecture is to study the bulk and surface properties of metal alloys *without* any experimental parameters as input. As already mentioned in the Introduction, we use Density Functional Theory (DFT)[12,13] as starting point for our studies. Although DFT permits one to calculate alloy properties with an accuracy that often allows for a quantitative comparison with experimental data, it is usually limited to a small subset of the configuration space. The geometric relaxation of unit cells consisting of more than 100 atoms already becomes extremely difficult, and even impossible for some cases. So, compared to the 2^N configurations of a binary system containing N atoms, we are restricted to a very small part of the parameter space. Normally, a set of "intuitive structures" is chosen and that with the minimal energy is postulated as ground-state configuration. This,

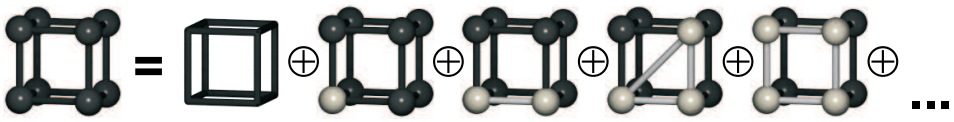

Figure 4. The concept of cluster expansions: The crystal is separated in characteristic figures (here, shown for the fcc-lattice). The energy of any configuration can then be written as linear combination of the characteristic energies J_f of the figures.

however, fails to allow for surprises, only one of the chosen input structures can result as ground-state. In order to circumvent this problem, the accuracy of DFT is extended to huge configuration spaces by combining DFT with concepts from statistical mechanics. The basic idea by Sanchez, Ducastelle and Gratias[14] is called "Cluster Expansion" (CE), and sketched in Fig. (4): For a given underlying lattice, the crystal structure is divided into characteristic figures such as pairs, triangles, etc. Then, the energy of *any* configuration σ on this lattice can be uniquely written[14] as linear combination of the characteristic energies J of each individual figure. In practice, the only error we make is that the sum must be truncated at some point. The Π_f's in Fig. (4) are structure-dependent factors and will be discussed in detail in section 2.2.

2 Methods

2.1 Elastic properties of alloys from density functional theory

Density functional theory (DFT) represents the probably most important many-particle approach in solid-state physics with respect to applications. Since there exists a number of excellent review articles (see e.g.[15,16]) and books (see e.g.[17–19]) about DFT, only some general remarks will be given: DFT is based on the Hohenberg-Kohn-theorem[12] stating that the energy of a system of interacting electrons in an external potential depends only on the ground state electronic density. In our case, namely the investigation of solid structures, the external potential is the Coulomb potential caused by the nuclei in a solid. The ground-state density can in principle be calculated from a variation ansatz, i.e. without any Schrödinger-equation, however for treating real problems the variational approach is unpracticable. Help came in 1965 by Kohn and Sham[13] who showed that the density wanted is given by the self-consistent solution of a set of single particle equations, called Kohn-Sham equations:

$$\left[-\frac{\hbar^2}{2m}\nabla^2 + V_{e-nuc}(\mathbf{r}) + V_H(\mathbf{r}) + V_{XC}(\mathbf{r})\right]\Psi_i(\mathbf{r}) = \epsilon_i\Psi_i(\mathbf{r}) \qquad (4)$$

In this Schrödinger-like equation, the first term on the left side represents the kinetic energy operator, V_{e-nuc} the Coulomb potential due to the nuclei, V_H the Hartree potential, and V_{XC} is the exchange correlation potential. The latter comes from replacing the kinetic energy of interacting particles by that of non-interacting particles (which can be treated exactly) plus a term containing all correlation and exchange effects (which is unknown, but small compared to the other energy contributions). Well-known approximations for

V_{XC} are the Local Density Approximation (LDA)[20,21] and the Generalized Gradient Approximation (GGA)[22] . In LDA, the energy density of the inhomogeneous system is approximated by the density of the *homogeneous* electron gas which possesses exactly the same density as the actual *inhomogeneous* system. Although this sounds like a very rough approximation, especially for systems with strongly varying density, it works astonishing well for a huge number of problems. In GGA, additionally the gradient of the density is considered which can be important for systems where $n(\mathbf{r})$ changes dramatically with $\mathbf{r}$.

In practice, we can distinguish between more or less two different types of strategies: Methods using complex, but efficient basis sets for the wavefunctions, as the Linearized Augmented Planewave method (LAPW) and methods based on so-called pseudopotentials (PP) using plane waves as basis set (for a survey see e.g. the book by Singh[23]). The concept of pseudopotentials is roughly spoken that most physical properties of a solid are determined by the valence electron structure. Then, the number of plane waves necessary to describe the system can be tremendously decreased by replacing core electrons and ionic potential by a pseudopotential which is energetically much weaker and corresponds to a node-free wavefunction. Thereby, the pseudopotential has to fulfil the conditions that (a) the scattering properties of the elements are conserved and (b) outside the core-region pseudopotential and pseudo-wavefunction are identical to the corresponding full potential and wavefunction. Until some years ago, it was a very delicate task to study transition-metals by "classical", norm-conserving pseudopotentials[24,25]. With the development of ultrasoft pseudopotentials[26,27] and more recently, so-called PAW-potentials ("Projector Augmented Wave")[28,29] concepts from LAPW entered in PP-codes and allow for an accurate and fast treatment of practically all metal-system by a plane wave basis set.

In many cases, results retrieved from DFT calculations are used as input for other numerical and analytic models to describe a certain class of properties of an alloy system. One important example is the use of the DFT energetics in elasticity theory in order to calculate the strain behaviour of metal alloys. In Subsection (2.2), we will see, how the following concept permits one to understand the size versus shape relation of characteristic microstructures in metal alloys. Since strain is determined by the mechanical behaviour of the system, we separate the two components by creating an interface in a well-defined orientation between A- and B-atoms and demand that the whole system act as a pseudomorphic, epitaxial system, i.e. there are no dislocations at the interface. The idea to compare a binary alloy with an epitaxial film/substrate system allows to specify two types of quantities[30]:
(i) The *hydrostatic deformation energy* $\Delta E_A^{hydro}(a)$ being the energy required to hydrostatically deform the solid element A to the lattice constant a of the alloy.
(ii) The *epitaxial strain energy* $\Delta E_A^{epi}(a, \hat{G})$, representing the energy of the elemental solid A epitaxially (or, biaxially) deformed to the "substrate" lattice constant a in the two directions orthogonal to $\hat{G}$ and *relaxed* along $\hat{G}$.
The ratio of these two energies defines the *epitaxial softening function*[30,31]

$$q(a, \hat{G}) = \frac{\Delta E_A^{epi}(a, \hat{G})}{\Delta E_A^{hydro}(a)}. \tag{5}$$

Since it is always easier to deform a material epitaxially (biaxially) than hydrostatically (triaxially), $q \leq 1$. Small values of $q(a, \hat{G})$ indicate elastically soft directions $\hat{G}$. As an example, Fig. (5)(b) shows calculated softening functions, $q(a, \hat{G})$, for the fcc-elements Al

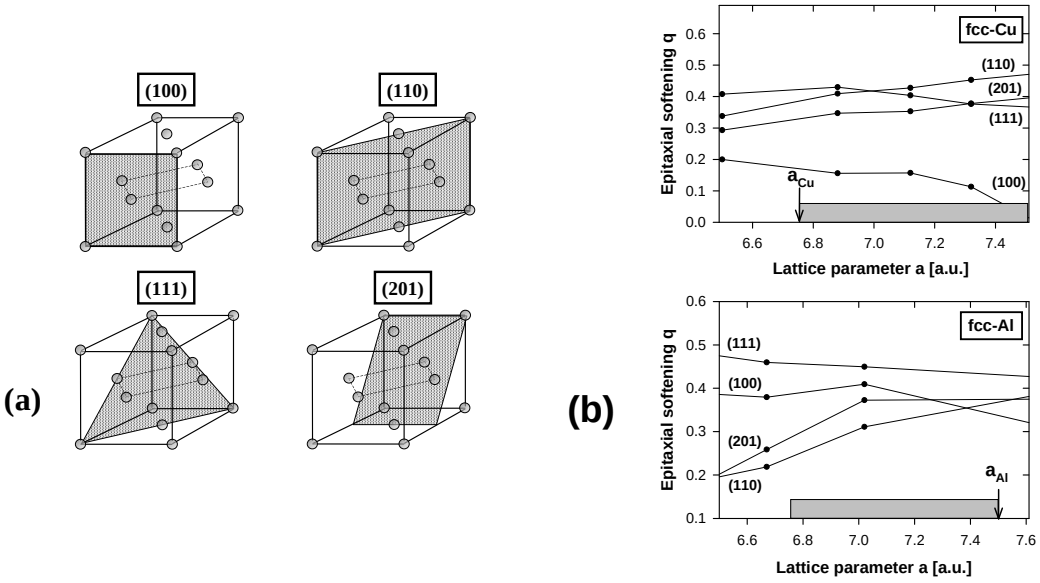

Figure 5. (a) Low index crystal orientations of the fcc-lattice indicated by hatched areas. (b) Epitaxial softening function $q(a, \hat{G})$, Eq. (5), for Cu and Al calculated via LDA. The shaded areas mark the lattice parameter range between the two components of the corresponding alloy. Arrows denote the position of the equilibrium lattice constant a_{eq} of each element. The lines are drawn merely to guide the eye.

and Cu along the crystal directions indicated in Fig. (5)(a). Obviously, the crystallographic order of elastic softness can change as function of the lattice parameter. For example, an only 2% compression of Al (Fig. (5)(b)) is softer along (110) than along (100), while at the equilibrium the opposite is true. This clearly indicates that for a description of strain effects in metals, not only the direction dependence of strain (*anisotropic* strain effects), but also the dependence of strain on the lattice parameter (*anharmonic* strain effects) must be taken into account[32,33]. In the harmonic elasticity theory, q depends only on the direction $\hat{G}$, but *not* on the substrate lattice constant a[30,34,35]:

$$q_{harm}(\hat{G}) = 1 - \frac{B}{C_{11} + \Delta\gamma_{harm}(\hat{G})} \tag{6}$$

with bulk modulus $B = \frac{1}{3}(C_{11}+2C_{12})$ and anisotropy parameter $\Delta = C_{44}-\frac{1}{2}(C_{11}-C_{12})$. The harmonic constants C_{11}, C_{12}, and C_{44} can be easily calculated from first-principles calculations[30] and consequently, Δ and B, too. γ_{harm} is a geometric function of the spherical angles Θ (polar angle) and Φ (azimuth angle) formed by $\hat{G}$:

$$\begin{aligned}\gamma_{harm}(\Phi,\Theta) &= sin^2(2\Theta) + sin^4(\Theta)sin^2(2\Phi) \\ &= \frac{4}{3}\sqrt{4\pi}\left[K_0(\Phi,\Theta) - \frac{2}{\sqrt{21}}K_4(\Phi,\Theta)\right]\end{aligned} \tag{7}$$

Here, K_l is the Cubic harmonic of angular moment l. If anharmonic effects become im-

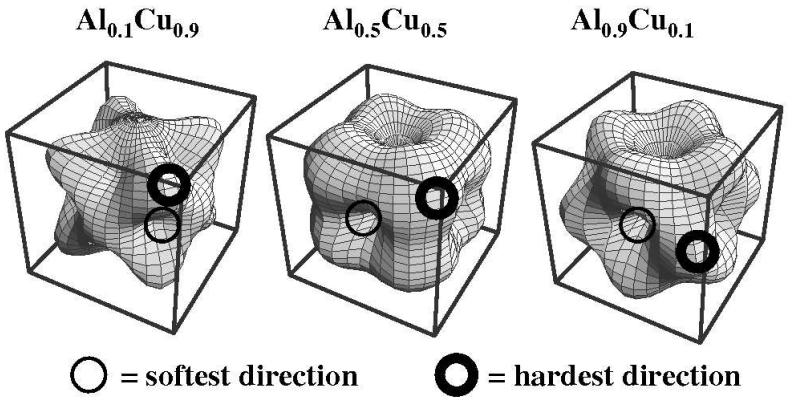

Figure 6. Parametric three dimensional presentation of the constituent strain ΔE_{CS}^{eq}, Eq. (10), of Al-Cu for compositions of 10%, 50%, and 90% Al. The distance from the surface to the centre of the cube represents the amount of the strain energy.

portant as in metal alloys, q additionally depends on the lattice parameter a:

$$\gamma(a,\hat{G}) = \gamma_{harm}(\hat{G}) + \sum_{l=0}^{l_{max}} b_l(a) K_l(\hat{G}). \tag{8}$$

This equation now also includes higher order cubic harmonics as necessary to go beyond the harmonic approximation (more details are given by Ozolins et al.[32]). Then, Eq. (6) becomes

$$q(a,\hat{G}) = 1 - \frac{B}{C_{11} + \Delta\gamma(a,\hat{G})}. \tag{9}$$

With $q(a,\hat{G})$ resulting from DFT calculations as displayed in Fig. (5)(b), the quantity $\gamma(a,\hat{G})$ can be taken from Eq. (9) and, in turn, the coefficients $b_l(a)$ results via Eq. (8). The determination of $b_l(a)$ permits one to generalize calculated epitaxial energies, $\Delta E_A^{epi}(a,\hat{G})$ for a discrete set of directions to *arbitrary* directions $\hat{G}$.

We will apply it to parameterize the equilibrium *constituent* (or *coherency*) *strain energy* $\Delta E_{CS}^{eq}(x,\hat{G})$ which is defined as the strain energy required to maintain coherency between a "piece" of material A and a "piece" of material B along an interface with orientation $\hat{G}$. This structure represents a so-called *superlattice* A_nB_n along a certain direction $\hat{G}$ with $n \to \infty$. In practice, the calculated elemental epitaxial energies are used to determine the constituent strain energy that is determined by the equilibrium value of the composition-weighted sum of the epitaxial energies of A and B:

$$\Delta E_{CS}^{eq}(x,\hat{G}) = \min_{a_p}[x\Delta E_A^{epi}(a_p,\hat{G}) + (1-x)\Delta E_B^{epi}(a_p,\hat{G})] \tag{10}$$

where $a_p(x)$ is the lattice constant that minimizes ΔE_{CS}^{eq} at each x. The constituent strain can be illustrated by a three-dimensional parametrization in terms of a sum of Kubic harmonics, as shown in Fig (6) for for three different Al-concentrations of the system Al-Cu.

Here, the distance from the surface to the centre of the cube represents the strain energy in this crystallographic direction. For $Al_{0.1}Cu_{0.9}$, we see that this distance is maximal along the body diagonal (marked by a bold circle), i.e. the crystallographic [111] direction, whilst the distance is shortest along the square face diagonal (marked by a thin circle), i.e. the [110] direction. With increasing Al composition the situation changes: $Al_{0.5}Cu_{0.5}$ owns the smallest constituent strain for [100], while [111] is still the hardest direction. For 90% Al, the figure has a "depression" in the very soft [100] direction, but a protrusion in the hard [111] direction. As we will see next, the concept of constituent strain is very important to describe morphological properties of alloys.

2.2 Controlling configuration space and length scales: The UNCLE code

As discussed in Section II, the idea of cluster expansions[14] is to express the atomically relaxed energy, $E(\sigma)$, of arbitrary lattice configurations σ on a given, underlying lattice as linear sum of energies characteristic of geometric figures, such as biatoms, triatoms, etc. (see Fig. (4)). To realize this idea, we transform the "alloy problem" to an Ising model. Each atom i of an $A_{1-x}B_x$ alloy is assigned to a spin-value $S_i = -1$, if i is an A-atom, and to $S_i = +1$, if i is a B-atom. Then, the energy of each configuration can be expressed by an Ising-expansion:

$$E(\sigma) = J_0 + \sum_i J_i S_i(\sigma) + \sum_{j<i} J_{ij} S_i(\sigma) S_j(\sigma) + \sum_{k<j<i} J_{ijk} S_i(\sigma) S_j(\sigma) S_k(\sigma) + ... \quad (11)$$

The first two terms on the right define the energy of the random alloy (with zero mutual interactions), the third term contains all pair interactions, the fourth all three-body interactions, etc. This equation can be brought to a compact form by introducing a correlation function $\bar{\Pi}_F$ for each class of symmetry-equivalent figures F[36]:

$$\bar{\Pi}_F(\sigma) = \frac{1}{N D_F} \sum_f S_{i_1}(\sigma) S_{i_2}(\sigma) ... S_{i_m}(\sigma) \quad (12)$$

Here, D_F gives the number of figures of class F per site. The index f runs over the ND_F figures in class F and m denotes the number of sites of figure f. Then, Eq. (11) becomes[35]

$$E(\sigma) = \sum_F D_F \bar{\Pi}_F(\sigma) J_F \quad (13)$$

The coefficients J_F of the cluster expansion are determined by fitting to an input database. This input database consists of a set of atomic configurations, whose energy has been determined, e.g., using ab-initio methods. An efficient cluster expansion method will facilitate the exchange of structural information between the fitting routines and the first-principles code. This decreases the amount of user time required and reduces the chances for human error.

Our new computer code UNCLE (UNiversal CLuster Expansion)[37] has been designed to adapt the output of the pseudopotential code VASP[27,28,38–40] and the FLAPW code FLAIR[41–43]. It should be mentioned though, that the source of the input values in the database can be arbitrary, and do not necessarily have to originate from first-principles calculations. For every input value in the database, the corresponding structural information is given as follows: real-space coordinates of the supercell B, the number of each

chemical atomic species in the cell, and positions of the basis atoms within the superstructure. The latter is given either in direct or Cartesian coordinates. Following the structural information, the corresponding value of the observable to be expanded is given.

After the input structures have been read in, UNCLE checks whether all their basis atoms lie on the lattice and whether there are symmetry-equivalent structures within the input list. As trivial as this step may seem, in practice this becomes an extremely useful feature; converged cluster expansions typically require around 50–150 input structures, which tend to contain subsets of similar, though symmetrically-distinct, atomic configurations. This can cause unintentional duplication of input structures, which not only wastes calculation time, but also falsely overweights the structure during the fitting.

The choice of atomic configurations, from which the effective cluster interactions are extracted, affects the ECIs. To avoid biasing the input database, and thus the ECIs, we systematically increase the database. We begin with a hand-chosen set $\{\sigma\}$ of usual suspects, small-unit-cell structures derived from the parent lattice, and some quasi-random structures. The first cluster expansion determined from this initial set makes predictions, perhaps not accurately, for the ground states and other structures with a "low" enthalpy of formation. One efficient tool to find structures with important "structure information" for the determination of the interactions is a ground-state search[44,45] in the early stage of the construction: For a "starting set" of about 20 DFT energies of arbitrary input-structures, a CE fit is performed. The resulting interactions are then used to predict the energy of *all possible structures* with e.g. up to 20 atoms per unit cell (the latter is indeed a very reasonable restriction, since most known stable structures in binary metal alloys own clearly less than 20 atoms per unit cell). Such an analysis based on Eq. (13) takes only some hours on a high-performance PC. Afterwards, the CE energies of all structures are plotted as function of composition, and a ground-state line is constructed. This is schematically shown in Fig. (7): An individual structure σ only contributes to the ground-state line, if the linear energy average between the stable structures at next higher and lower concentration is energetically less favourable than the energy of σ. More precisely, for three structures α, σ and β with $x(\alpha) < x(\sigma) < x(\beta)$ which are the lowest in energy for their individual concentrations, the structure σ has to fulfil the condition

$$E(\sigma) < \frac{x(\sigma) - x(\beta)}{x(\alpha) - x(\beta)} E(\alpha) + \frac{x(\sigma) - x(\alpha)}{x(\beta) - x(\alpha)} E(\beta) \tag{14}$$

in order to be the ground-state at $x(\sigma)$. If Eq. (14) holds, a mixture of the phases α and β would be higher in energy than structure σ. With the ground state line constructed, UNCLE automatically checks for all structures which lie on it, whether they are already considered as input structures for the CE. If not, their DFT energy is calculated and added to the input-structure set. This cycle is repeated, as shown in Fig. 8, letting the current cluster expansion itself pick new structures to add to the database.

In practice, the prediction of the energy (or any other observable) over a system's configuration space (e.g., ground state searches) by the help of UNCLE requires only minimal user input. We have implemented an algorithm[46] that automatically generates all possible atomic configurations within all geometrically possible supercells for an arbitrary number of basis atoms on a given lattice. The algorithm removes all symmetry-equivalent structures and still scales linearly with the number of unique configurations. For a ground state search based on the cluster-expansion Hamiltonian, Eq. (13), the user only has to provide

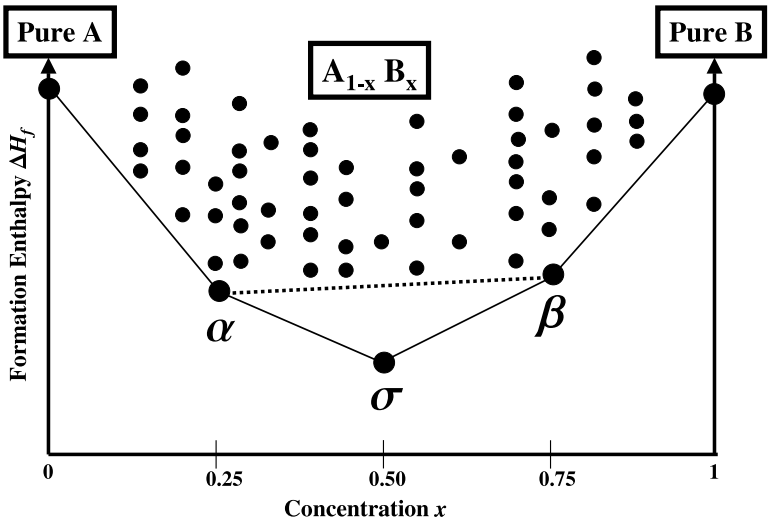

Figure 7. Schematic ground-state diagram of a binary alloy $A_{1-x}B_x$. The ground-state line was constructed from 60 energies of relaxed structures (given by dots) by use of Eq. (14). Besides the pure elemental crystal the ground-state line is formed by three structures α, σ, and β for concentrations $x = 0.25, 0.50$, and 0.75, respectively. If σ would lie energetically above the dashed tie line between α and β, a mixture of α and β would be more stable than σ.

(i) the maximum number of basis atoms up to which configurations are to be considered and (ii) the figure set chosen by a previous genetic algorithm run, along with the corresponding effective cluster interactions J. With this input, UNCLE automatically generates all possible superstructures (configurations) and determines their energy as predicted by the cluster expansion. The resulting ground state diagram and convex hull essentially constitute the $T = 0$ K phase diagram of the system.

We apply a new mathematical formalism to the cluster expansion that considerably simplifies aspects. Two places where this is particularly useful is in calculating the correlations (needed to perform the sum in Eq. (13)) and in Monte Carlo simulations. The new formalism works in the "space" of 3×3 *integer* matrices and provides an alternative representation for structures and figures.

Any supercell of the parent lattice is an integer multiple of the parent cell. So if the vectors of the parent lattice are the column vectors of a matrix A, there exists a matrix N, with all integer elements, such that $B = AN$. The columns of B are the lattice vectors of the supercell and the determinant of N will be the multiplicative factor; that is, if the supercell has twice the volume of the parent cell, then $|N| = 2$.

Because $B = AN$, the integer matrix N is an alternative representation for the superlattice. Realizing this, we can then map the superlattice and its atomic sites to this alternate representation, the g-representation, where the calculation of correlations is greatly simplified. In the g-representation, the atomic sites lie on an integer lattice, $\mathbb{Z}^3$, and the shape of the supercell is always orthorhombic. This simplifies the algorithm and thus makes the code much more efficient, both in time and memory.

Mapping to the g-representation is accomplished by decomposing N into its Smith

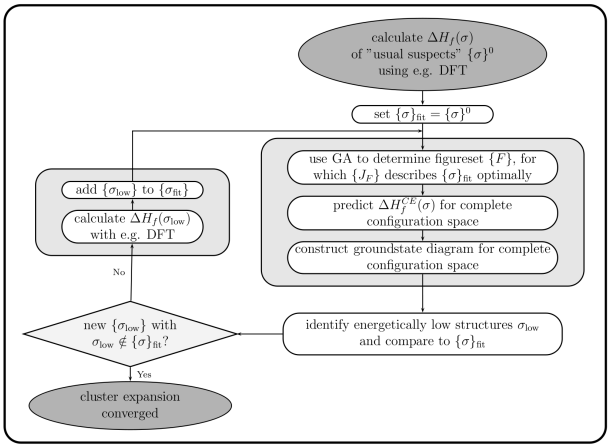

Figure 8. Illustration of the self-consistent "outer loop", which chooses the input structures of the cluster-expansion.

normal form (SNF). The SNF is a diagonal form with special properties (for details, see ref.[46,37]). and forms the key for efficient computation of correlation:. The lattice vectors and lattice points are represented by integers rather than floating point variables. No logic statements in the loops are required; no comparison of floating point numbers are needed. This improves both the efficiency and the robustness of the implementation.

Our implementation of UNCLE can be generalized to treat multinary systems. The treatment of ternary compounds has already been implemented and used. The extension beyond ternary systems is relatively simple and will be made as soon as required. To handle multinary expansions, the correlations must be calculated over a set of cluster functions. Formally there is also a set of cluster functions for a binary expansion, but there is only one function in the set and it can be taken to be the occupation itself, that is $\theta(s_i) = s_i$.

In the binary case, the correlation is computed merely by taking the product of each occupation value (± 1) over each vertex of a figure:

$$\Pi = \prod_{i=1}^{k} s_i \tag{15}$$

and there is one ECI, J, for each figure. But in the case of a n-ary system (n-components represented by n spin values), the complete description of the correlations requires $(n-1)$ cluster functions θ_l. Therefore, a figure with k vertices is no longer connected with a single correlation function, but instead $(n-1)^k$ correlation functions $\Pi^{(j)}$. The i^{th} entry of the superscript vector (j), which contains k entries, defines the cluster function θ_l, which is to be applied to the i^{th} vertex of the figure

$$\Pi^{(j)} = \prod_{i=1}^{k} \theta_{l=(j_i)}(s_i) \tag{16}$$

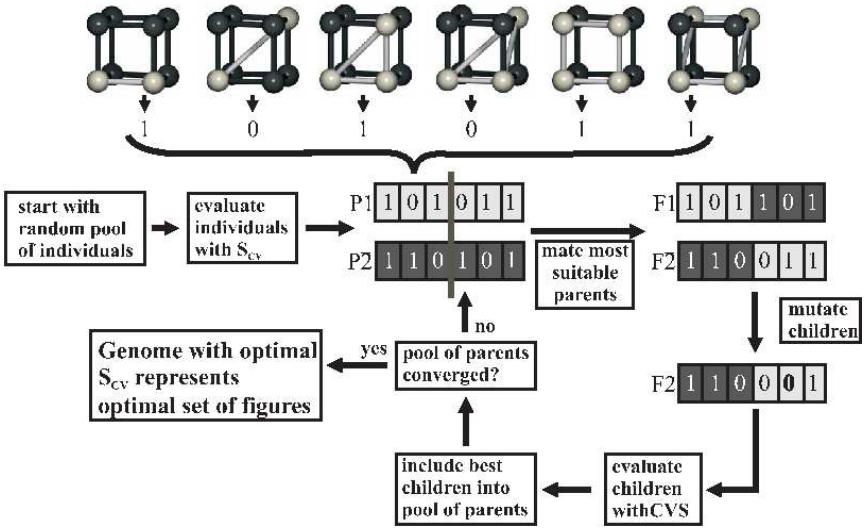

Figure 9. Illustration of the Genetic Algorithm, which helps to safely identify the relevant figures that need to be included in the CE-sum.

The full set of correlation functions of a figure consists of all the 2^k possible vectors (j). This number can be reduced according to the symmetry of a figure. The general multinary formalism was laid out by Sanchez et al. in[14], and later applied by Wolverton and de Fontaine[47]. Along the lines of the latter, we use Chebychev polynomials as cluster functions in the ternary case, an example for their application is given in section 3.2.

The cluster expansion approach is exact only when all possible figures are included in the cluster expansion sum, Eq. (13). But including such an (astronomic) number of terms in the expansion is impractical. To be useful, the expansion must be truncated to a relatively small number of terms without losing the expansion's predictive power. Choosing which figures to retain is the most critical step of the cluster expansion method. Nevertheless, finding a good selection of figures is a formidable task: There may be thousands of figures to choose from. Selecting a few dozen interactions from a pool of thousands is impossible to do exhaustively.

So far an evolutionary approach based on a genetic algorithm (GA) has proven to be the most effective way to choose the figures. The set of figures chosen by the GA results in a cluster expansion that has better predictive power than if chosen using other approaches. The details of the algorithm, which is implemented in UNCLE, have been described in[48,49]. Its basic principle is illustrated in Fig. 9.

The fitness criterion for the selection of figures is a *leave-many-out* cross validation score (see e.g.[50,51]). This fitness score S_{CV} is a measure of the predictive power for a given choice of figures. Its value is calculated by the following scheme:

1. Randomly choose $\mathcal{N}$ sets $\{\sigma\}^i_{\text{prediction}}$, $(i \in \{1...\mathcal{N}\})$ of n different structures out of the total pool of input structures.

2. For each of the $\mathcal{N}$ prediction-sets $\{\sigma\}^i_{\text{prediction}}$, perform a cluster expansion based

on all input structures except for those contained in $\{\sigma\}^i_{\text{prediction}}$. The resulting ECIs are not influenced by the energetics of $\{\sigma\}^i_{\text{prediction}}$.

3. Use the resulting ECIs to predict the energy of every member of $\{\sigma\}^i_{\text{prediction}}$ and compare it to the energy calculated by density functional theory.

4. Calculate the expectation value of the root-mean-square error for all the predicted structures:

$$S_{\text{CV}} = \sqrt{\frac{1}{\mathcal{N} \cdot n} \sum_{\mathcal{N}} \sum_{n} |E_{DFT}(\sigma) - E_{CE}(\sigma)|^2} \tag{17}$$

Other successful applications of the genetic algorithm within a cluster expansion can be found, e.g., in Ref.[52]. The GA has already been compared to the tetrahedron method proposed in[53] and the Variational Cluster Expansion[54,55], and proved to be the most reliable in finding the choice of figures with the best S_{CV}.

The determination of Effective Cluster Interactions (ECI) is performed as follows: For a given choice of figures and a set of $\mathcal{N}$ input structures $\{\sigma\}$, the effective cluster interactions J are extracted by minimizing[56]

$$\sum_{\mathcal{N}} \left(E_{DFT}(\sigma) - \sum_{F} D_F J_F \overline{\Pi}_F(\sigma) \right)^2 + \sum_{F} t_F J_F \stackrel{!}{=} \min \ , \tag{18}$$

where the last term is a *damping* term, which penalizes figures with large spatial extent (the spatial extent is determined as the average distance of the vertices from a figure's center of mass) $\mathbf{r_F}$:

$$t_F = c \cdot (\mathbf{r_F})^{\lambda} \tag{19}$$

The scaling variables c and λ are set independently for pair figures and higher-order figures. They are *not* chosen by the user, but optimized within the genetic algorithm.

For the fitting of the interactions according to equation 18, a set of constraints is introduced as proposed by Garbulsky and Ceder[57]. These constraints maintain the energetic hierarchy of the input structures within the hierarchy of the predicted energetics:

$$\Delta H^{\text{DFT}}(\sigma) - \delta_1(\sigma) < \Delta H^{CE}(\sigma) < \Delta H^{\text{DFT}}(\sigma) + \delta_1(\sigma) \tag{20}$$

$$\Delta H^{\text{DFT}}_{\text{GSL}}(\sigma) - \delta_2(\sigma) < \Delta H^{CE}_{\text{GSL}}(\sigma) < \Delta H^{\text{DFT}}_{\text{GSL}}(\sigma) + \delta_2(\sigma) \tag{21}$$

$$\Delta H^{\text{DFT}}_{\text{lowest}}(\sigma) - \delta_3(\sigma) < \Delta H^{CE}_{\text{lowest}}(\sigma) < \Delta H^{\text{DFT}}_{\text{lowest}}(\sigma) + \delta_3(\sigma) \tag{22}$$

The first constraint simply requires that the enthalpy $\Delta H(\sigma)$ of every structure σ, as calculated by DFT and predicted by the CE, matches within the error bars $\delta_1(\sigma)$. Independent error bars $\delta_i(\sigma)$ are set up for the energy distance of the enthalpy of a structure to the value of the ground state line at the respective concentration $\Delta H_{\text{GSL}}(\sigma)$, as well as for the energy distance between a structure's enthalpy and the enthalpy of the energetically lowest structure at this concentration $\Delta H_{\text{lowest}}(\sigma)$. For the actual fitting of Eq. (18) within the constraints of Eq. (20), an algorithm proposed by Goldfarb and Idnani[58] is implemented.

In some cases it may be more important to conserve the energy hierarchy for low-energy input-structures than for less stable structures. Thus, the error bars $\delta_i(\sigma)$ defined

in equation 20 depend on each structure's energy difference to the lowest structure at the respective concentration $\Delta H^{DFT}_{\text{lowest}}(\sigma)$, determined from first principles:

$$\delta_{\{1,2,3\}}(\sigma) = \delta^{\text{const}}_{\{1,2,3\}} \cdot \exp\left(-\frac{\Delta H^{\text{DFT}}_{\text{lowest}}(\sigma)}{k_B \cdot T}\right) \quad , \tag{23}$$

The constant part $\delta^{\text{const}}_{\{1,2,3\}}$ is specified at runtime. The Boltzmann-like energy-dependence can be varied through the term $k_B T$, and effectively turned off if desired.

While the fitting process is automatic, it introduces a set of new parameters for the fit itself (c and λ) as well as the Garbulsky-Ceder constraints. While the variables c and λ are optimized automatically within the genetic algorithm, $\delta_i(\sigma)$ and $k_B T$ have to be specified by the user. Nevertheless, it is simple to make sure that the constraints are set correctly by checking if the hierarchy predicted by the cluster expansion correctly reflects the hierarchy as determined by density functional theory. If this is not the case, then the constraints are lowered until the energetic hierarchy is preserved.

The selection and determination of the effective cluster interactions becomes challenging for low-symmetry systems such as surfaces. In the case of a surface, there is a loss of *translational* symmetry in one dimension. Consequently, the number of independent figures increases significantly because the ECIs become *layer dependent*. Compared to a bulk case, a larger number of input structures is necessary in order to determine the ECIs. However, it is possible to circumvent a part of this problem by treating the surface interactions as "correction" of the bulk interactions.

Because energies are additive, we may write

$$\Delta H^{CE}_f = \Delta H^{Vol}_f + \Delta H^{Surf}_f. \tag{24}$$

This ansatz was first applied by Drautz et al. to study the energetics of Ni-rich Ni-Al surfaces[59]. The advantage in treating the surface interactions as *correction* of the bulk interactions comes from the fact that the DFT calculations for different surface terminations and segregation profiles do not have to account for an infinite bulk reservoir. We only have to make sure that the DFT slab model is thick enough that the center layer of the slab is bulk-like. The energy of a structure σ can then be written as

$$E(\sigma) = \sum_{i=1}^{N} \left\{ \sum^{N_F} d_F \overline{\Pi}_F(\sigma) J_F + \sum^{N'_F} d'_F(\mathbf{R}_i) \overline{\Pi}'_F(\mathbf{R}_i) \delta J_F(\mathbf{R}_i) \right\}. \tag{25}$$

We see that for the surface part the interactions become site dependent. Here, $\mathbf{R}_i$ defines the position of the atom i with respect to the alloy surface. So, for an atom i within the segregation profile, every individual interaction J_F to neighboring atoms will be corrected to $J_F + \delta J_f(\mathbf{R}_i)$. Naturally, with increasing distance from the alloy surface, $\delta J_F \to 0$ and consequently the surface term (second term) in Eq. (25) becomes zero. In the case of e.g. a $Pt_{25}Rh_{75}(111)$ surface it turned out $\delta J_F \to 0$ already by the fourth layer[52,60].

In practice, for more complex surface problems, even this partition of the energy may be an insufficient strategy. In some cases, finding a sufficiently predictive set of ECIs may still require an unreasonably large number of DFT calculations. We are currently developing an additional concept to be implemented in UNCLE that will provide an improved reference energy as starting point for surface investigation. The mixed space cluster expansion[35,36] is applied to incorporate strain effects into the reference energy part. Next,

the energies of individual surface configurations are built from fully relaxed 1×1 surface structures, and, again, added to the reference energy part. We call this the concept of "structural bricks". After its implementation, it will be described in detail in Ref.[61].

There remains one critical point: As shown by Laks et al.[35], any CE in real space *fails* to predict the energy of long periodic coherent superlattices. For a given superlattice A_nB_n, Eq. (13) predicts a formation enthalpy $\Delta H_f = 0$ as $n \to \infty$. This indeed is an intrinsic fault of any finite CE and easy to understand: If we consider an A atom of an A_nB_n superlattice "far" away from the A/B interface so that all figures f connect the A atom exclusively to other A atoms, then the finite CE interprets the A atom as a bulk crystal atom and consequently, $\Delta H_f = 0$. However, as discussed in Section III.A, the formation enthalpy of an infinite superlattice should be defined as the equilibrium constituent strain energy, because in the limit $n \to \infty$ the superlattice formation enthalpy depends only on its strained constituents, and not on the interface properties. The problem can be solved[36,35] by transforming a group of interactions to the reciprocal space and adding the constituent strain term explicitely. This is easiest to do for the pair interactions. For this, we introduce the Fourier transform of real-space pair interactions, $J_{pair}(\mathbf{k})$ and the structure factor $S(\mathbf{k}, \sigma)$:

$$J_{pair}(\mathbf{k}) = \sum_j J_{pair}(\mathbf{R}_i - \mathbf{R}_j) \exp\left(-i\mathbf{k}\mathbf{R}_j\right) \tag{26}$$

$$S(\mathbf{k}, \sigma) = \sum_j S_j \exp\left(-i\mathbf{k}\mathbf{R}_j\right) \tag{27}$$

Then the formation enthalpies for any arbitrary atomically relaxed configuration σ are expressed by[36]

$$\Delta H_{CE}(\sigma) = \sum_{\mathbf{k}} J_{pair}(\mathbf{k}) |S(\mathbf{k}, \sigma)|^2 + \sum_F D_F J_F \bar{\Pi}_F(\sigma) + \Delta E_{CS}(\sigma). \tag{28}$$

This solution was introduced by Zunger and co-workers[36,35] and is called *Mixed-Space Cluster Expansion* (MSCE). The first term includes all pair figures in **k**-space. The second term represents many-body interactions and runs over symmetry inequivalent clusters consisting of three or more lattice sites. It also includes J_0 and J_1 from Eq. (11). D_F again stands for the number of equivalent clusters per lattice site, and $\bar{\Pi}_F(\sigma)$ are the structure-dependent geometrical coefficients given by Eq. (12). The last term represents the constituent strain energy of the structure σ, $\Delta E_{CS}(\sigma)$, and can be calculated by expanding the equilibrium constituent strain energy (Eq. (10)), $\Delta E^{eq}_{CS}(x, \hat{k})$, as[35,62]

$$\Delta E_{CS}(\sigma) = \sum_{\mathbf{k}} J_{CS}(x, \hat{k}) |S(\mathbf{k}, \sigma)|^2 \tag{29}$$

with

$$J_{CS}(x, \hat{k}) = \frac{\Delta E^{eq}_{CS}(x, \hat{k})}{4x(1-x)}. \tag{30}$$

Now, J_{CS} contains the correct long-periodic superlattice limit, namely the constituent strain energy [a].

[a] It has been found[62] that attenuating the constituent strain term can be important in strongly anharmonic, ordering

2.3 Extension to finite temperature and time-dependent properties

For finite temperature studies, Eq. (28) can be used in Monte-Carlo simulations. The code we applied for studying thermodynamic properties is a simple Metropolis algorithm[63] allowing for flipping pairs of A and B atoms in *arbitrary* distance mutual with the aim to reach the equilibrium configuration as fast as possible. The procedure is as follows:

1. Select randomly a pair of A and B atoms.
2. Calculate the energy difference δE caused by exchanging the two atoms. If $\delta E < 0$, flip the two spins; if $\delta E > 0$, flip the two spins with a probability of $\exp(-\delta E/kT)$ [again, E is obtained from Eq. (28)].
3. Go to 1.

Besides the temperature dependence of the alloy's free energy, MC simulations can be used to calculate coherent phase boundaries in the phase diagram. Following the fluctuation-response theorem[64] , the specific heat c_v of the system at a certain temperature can be calculated by the fact that c_v is proportional to the equilibrium fluctuations of the energy, $\langle E^2\rangle - \langle E\rangle^2$. Since the energy exhibits a point of inflection for a second-order phase transition at the transition temperature T_{trans}, its response function $c_v = (\partial E/\partial T)_v$ has a maximum at T_{trans} (Fig. (10)(a)). Although a phase transition is –strictly spoken– only defined for an *infinite* system, one usually also speak from a phase transition of a *finite* system, given by the maximum of c_v at the transition temperature as illustrated in Fig. (10)(a). If the MC simulations are applied for different concentrations x, the resulting T_{trans} values can be used to construct the coherent phase boundary of a system as displayed in Fig. (10)(b) for the Al-rich side of the Al-Cu phase diagram[65]. The open circles are measured values[66]. A small piece of the incoherent phase boundary is also shown. Yet, this boundary cannot be calculated by our method which is restricted to *coherent* alloy problems.

Another important application of MC simulations is the prediction the system's ordering. Of special interest are short-range order effects in disordered alloys which can quantitatively expressed in terms of SRO parameters as introduced in Section 1. For this, we rewrite Eq. (3) to the equivalent form

$$\alpha_{lmn}(x) = 1 - \frac{P_{lmn}^{A(B)}}{x} \tag{31}$$

where $P_{lmn}^{A(B)}$ is the conditional probability that given an A atom at the origin, there is a B atom at (lmn). For comparison with experimental data, the so-called "shells" lmn are introduced which are defined by the distance between A and B atoms in terms of half lattice parameters, $(l\frac{a}{2}, m\frac{a}{2}, n\frac{a}{2})$, e.g. for an fcc-lattice the nearest-neighbor distance would be described by the shell (110), the second neighbor distance by (200) and so on. As already mentioned, the sign of α indicates whether atoms in a given shell prefer to order ($\alpha < 0$) or cluster ($\alpha > 0$). The SRO parameter may be written in terms of the cluster expansion pair correlations as[32]

$$\alpha_{lmn}(x) = \frac{\langle \bar{\Pi}_{lmn}\rangle - q^2}{1 - q^2} \tag{32}$$

type systems. This is realized by an exponential damping function. However, since attenuating the constituent strain has no significant effect on the systems considered in this paper, this will be not discussed here.

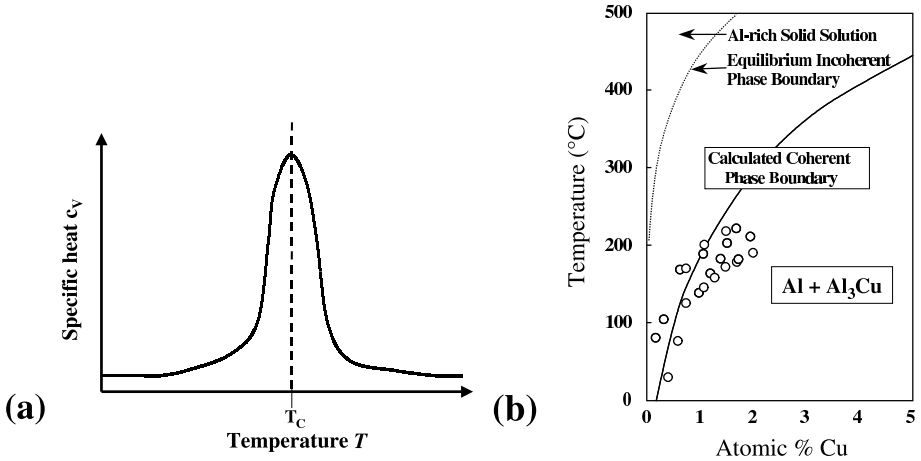

Figure 10. (a) Specific heat as function of temperature near a second-order phase-transition. c_v exhibits a maximum at T_{trans}. (b) Calculated coherent phase boundary for Al-rich Al-Cu and comparison to experimental data[66] (open circles).

where $q = 2x - 1$ and $\langle \bar{\Pi}_{lmn} \rangle$ is the pair correlation function, Eq. (12), for shell (lmn). In diffraction experiments the diffuse scattering due to SRO is proportional to the lattice Fourier transform of $\alpha_{lmn}(x)$[9,10]

$$\alpha(x, \mathbf{k}) = \sum_{lmn}^{n_R} \alpha_{lmn}(x) e^{i \cdot \mathbf{k} \cdot \mathbf{R}_{lmn}} \tag{33}$$

where n_R stands for the number of real space shells used in the transform. Equation (32) together with (33) opens the possibility to compare both, experimental and theoretically predicted diffuse diffraction patterns (reciprocal space) and SRO-parameters (real space). This concept will be applied in Section 3.1 to understand SRO phenomena in binary metal alloys *quantitatively*.

Similar to the calculation of the input structures' correlations for the cluster expansion, the determination of the starting energy of the Monte Carlo cell is done within the g-representation provided by the Smith normal form. The Monte Carlo cell is thus represented by the tensor G. Changing the atomic occupation of a site corresponds to changing the corresponding integer value of one element of G. In a Monte Carlo simulation, the calculation of the energy changes due to changes in the occupation (atom swaps) can be computed efficiently as only the energy contribution of those interactions "touched" by the swapped sites needs to be evaluated. The tensor G is the only large entity stored at runtime, requiring only *one byte* per site within the Monte Carlo cell; the correlations do *not* have to be stored at runtime. The minimal memory footprint allows for Monte Carlo cells of billions of sites, cpu time, rather than memory, becoming the limiting factor. A parallel implementation is planned to take advantage of this approach.

Besides the problem of bridging length scales, many materials properties require simulation times reaching from fractions of a second to weeks. One important example is the decomposition of an alloy into its constituents by precipitation. Precipitates represent

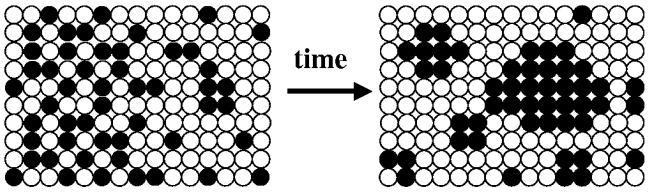

Figure 11. Schematic crystal-plane of an $A_{1-x}B_x$ alloy with characteristic islands formed by B (black) atoms during the aging process.

an important part of the microstructure of many alloy systems. Hereby, the dynamic evolution of precipitates takes place on a time scale of several hours, days or even months (see e.g.[69, 45]). The CE Hamiltonian can help to solve this second scaling problem, too, by using the effective interactions in Kinetic Monte-Carlo (KMC) simulations which is one of the most successful approaches to describe diffusion, growth and microstructure evolution in alloy systems[67]. The combination of CE and KMC simulations can be applied to simulate the aging of coherent precipitates in binary alloy systems. This decomposition reaction is sketched in fig. (11) by a simplified two-dimensional presentation: A quenched solid-solution (left frame) is aged at a given temperature. During this aging process islands are formed (right frame) which may show a characteristic size- and shape distribution (it is assumed that islands are formed by black B-atoms in an A-rich $A_{1-x}B_x$ alloy). The question is whether the distribution of these islands as a function of aging time can be calculated from first-principles.

The activations barrier for the exchange process can be expressed in terms of the temperature-dependent diffusion constant $D(T)$. In order to calculate $D(T)$ by a first-principles approach, it is assumed that the exchange of atoms is given by a vacancy-controlled diffusion. Therefore, in a first step, activation barriers must be calculated as a function of the structural environment. In the case of precipitation in which the alloy contains only a tiny amount (typically 1-5%) of the precipitating element, one often restricts the calculation of activation barriers to the case of the dilute limit (atom B in an A crystal) and the structural environment at the interface between solid-solution and precipitate. Although such activation barriers can -in principle- directly be used in KMC programs, they do not allow for a consideration of the temperature dependence as well as a transformation to real time scales. For this purpose, the complete phonon spectra for the relaxed structure corresponding to the vacancy formation, migration and the final configuration have to be calculated. This might be used in the framework of a transition state theory to predict the temperature dependent diffusion constant of the system, $D(T)$. Following classical diffusion theory the exchange frequency is proportional to the square of the atomic distance divided by the diffusion constant and the number of possible "jump directions" (e.g. six in a simple cubic lattice). If an exchange process between two certain neighbored atoms has been already chosen, then, consequently, the frequency $1/\tau_0$ for a chosen exchange process as a function of temperature T is connected to $D(T)$ by the relation

$$\tau_0(T) = \frac{a_{nn}^2}{D_{exp}(T)}, \tag{34}$$

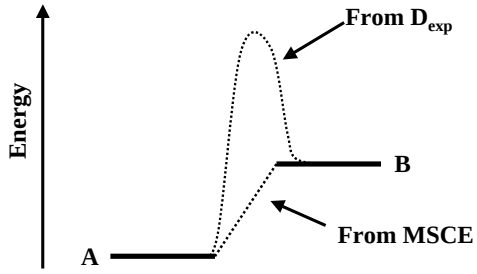

Figure 12. Basic assumption in our simulations[45]: While the energy difference between two neighboring atoms can be easily derived from the MSCE, an average and temperature dependent activation barrier is calculated from experimental temperature dependent diffusion data.

with a_{nn} being the average nearest-neighbor distance between atoms. Now, one can easily transform KMC steps to real time.

The strength of the CE to control a huge configuration space can now be utilized to calculate the energy difference for *all possible exchange processes* even, if there a millions of them. This allows to force atoms to move and to calculate the time which corresponds to this individual exchange process. The more unlikely an exchange process is, the longer is the corresponding time for this process. The concept is related to the "residence-time algorithm"[68] as discussed in chapter 12. for nearest-neighbor exchange processes only[69].

For the analysis of the shape of nanoclusters and precipitates, it is often helpful to apply the mixed-sace form of the cluster expansion (MSCE), because it allows for a quantitative separation of chemical and elastic energy parts[70]. Then, an accepted spin-flip would demand a recalculation of $S(\mathbf{k}, \sigma)$ in eqn. (28). However, as shown by Lu et al.[71], the MSCE method helps to avoid the necessity of recalculating $S(\mathbf{k}, \sigma)$ after each atomic movement by directly calculating the *change* in $J_{pair}(\mathbf{k})|S(\mathbf{k}, \sigma)|^2$ for each movement in real-space[71]. In the applied algorithm, a single KMC step is now *not longer a constant real time unit*, but depends on the corresponding probability W_{tot}. A single kinetic MC step corresponds indeed to only a single exchange of one B atom with one A atom and *not* to one trial-flip for each B atom. Since the "flip channel" i is always chosen randomly and usually a large number of B atoms (typically $10^3 - 10^5$) is considered to describe real aging processes, the probability that the same B atom is chosen in step i -when chosen already in step $(i-1)$- is extremely small. Due to the large system size it is not necessary to forbid certain exchanges between A and B atoms, i.e. we do not have to give up the restriction that the algorithm should be based on the Markovian process.

3 Applications

3.1 Ground-state search and short-range order

Our notions of the phase stability of compounds rest to a large extent on the experimentally assessed phase diagrams. Long ago, it was assumed that in the Cu-Pd system for

Name	$L1_2$	S1	S2 (LPS 3)	S3
Crystal structure	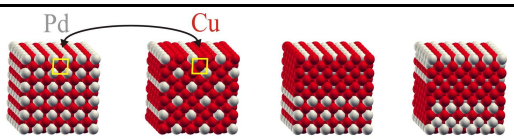			
	Cu_3Pd	Cu_7Pd	Cu_9Pd_3	Cu_8Pd_4
x_{Pd}	1/4	1/8	1/4	1/3
Lattice vectors	$\begin{pmatrix} 1&0&0\\ 0&1&0\\ 0&0&1 \end{pmatrix}$	$\begin{pmatrix} 1&0&0\\ 0&1&1\\ 0&\overline{1}&1 \end{pmatrix}$	$\begin{pmatrix} 1&0&0\\ 0&1&0\\ \frac{1}{2}&\frac{1}{2}&3 \end{pmatrix}$	$\begin{pmatrix} 1&0&0\\ 0&1&0\\ \frac{1}{2}&\frac{1}{2}&3 \end{pmatrix}$

Figure 13. [Color online] The ground state structures S1, S2 and S3, all related to $L1_2$ directly or to an $L1_2$-superstructure incorporating antiphase boundaries. These structures belong to the space group $P\frac{4}{m}mm$ (i.e. D^1_{4h} in Schoenflies nomenclature).

$x_{Pd} \leq 25\%$ there are at least two phases at high temperature ($L1_2$ and a $L1_2$-based superstructure), which evolve into a single, $L1_2$-ordered phase at low temperature. By constructing a first-principles Hamiltonian via the approach described above, a yet undiscovered Cu_7Pd ground state at $x_{Pd} = 12.5\%$ (referred to as S1 below) and an $L1_2$-like Cu_9Pd_3 superstructure at 25% (referred to as S2). We find that in the low-temperature regime, a single $L1_2$ phase cannot be stable, even with the addition of anti-sites. Instead we find that an S2-phase with S1-like ordering tendency will form. Previous short-range order diffraction data is quantitatively consistent with these new predictions (details can be found in ref.[72,73]). This study exemplifies how even well-established phase phenomena in classic alloy systems can be challenged via first principles statistical mechanics and calls for further experimental examination of this prototypical system.

Figure 14 shows the energies of $\approx 2^{20}$ ordered configurations and indicates the breaking points of the convex hull, i.e. the ground state structures. Figure 13 gives the structural description of the ground states. We find (a) The Cu_7Pd (S1) structure at $x_{Pd} = 12.5\%$, (b) the Cu_3Pd (S2 or LPS 3) structure at 25% and (c) the Cu_8Pd_4 (S3) structure at $x_{Pd} = 33\%$. We find that at $x_{Pd} = 25\%$ and $T = 0\,K$ S2 is considerably stabilized over $L1_2$ as ground state.

Finding (b) is in agreement with Refs.[74,75,71,76] ; S2 is predicted as a ground state at $x = 1/4$, lower in energy than $L1_2$: $\Delta H_f(S2) = -102.6\,meV/atom$, $\Delta H_f(L1_2) = -99.8\,meV/atom$. At 12.5% Lu *et al.*[77] predicted the D1 structure, which, though not identical to S1, is also similar to $L1_2$. The S1 ground state is related to the $L1_2$ structure by a simple exchange of Cu and Pd rows along $[100]$ as shown in Fig. 13. Previous studies (e.g.[78–80]) that obtained $L1_2$ as ground state at $\approx 18\%$ referred to the ANNNI Ising model, or performed an electronic mean field approach[74]. However, negligence of S1 in the first-principles input (Ref.[76]) will favour interactions that are "blind" for S1.

Given that we predict at an S1 phase $T = 0\,K$ at 12.5% Pd and an S2 phase at 25% Pd, it is interesting to characterize the phase(s) at intermediate concentrations. In order to examine the energies $E_{CE}(\sigma)$ of structures with cells bigger than 20 atoms (Fig. 3), we

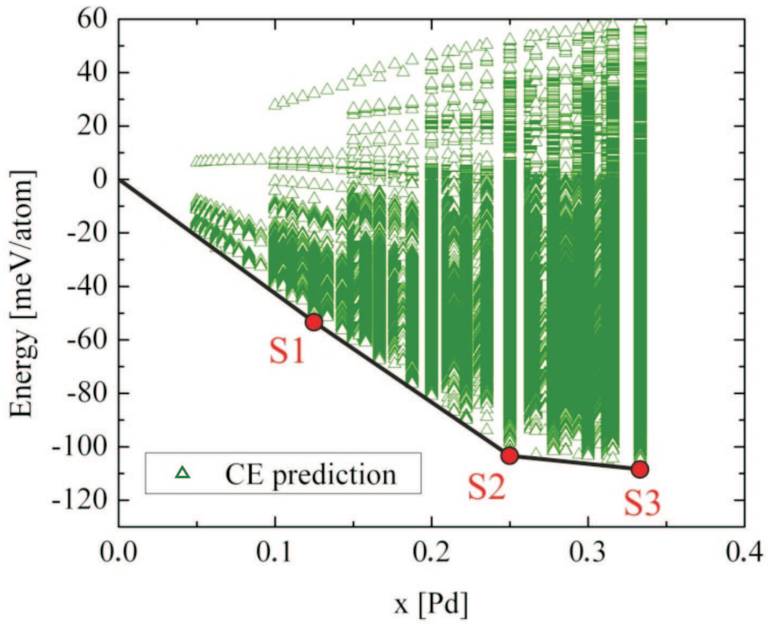

Figure 14. [Color online] Ground state diagram in the Cu-rich regime. Each triangle represents the predicted energy for one specific crystal structure. The solid line is the convex hull of all $\mathcal{O}(10^6)$ energies. The ground state structures are depicted in Fig. 13. $L1_2$ is not a ground state, but rather the $L1_2$-related superstructure S2 (LPS 3).

constructed large 24×24×24 cells and sample their energies via Monte Carlo (vibrational entropy was not taken into account). Due to the variety of incommensurate superstructures with non-coherent phase boundaries, we have to restrict our study to low temperatures [b]—a more thorough thermodynamic study may not be feasible with Monte Carlo. Nevertheless, the critical temperature $T_c \approx 800\,\mathrm{K}$ for the phase transition from A1 to S2 is in good agreement with experiment ($T_c^{\mathrm{Exp.}} \approx 780\,\mathrm{K}$). Simulated annealing in the intermediate region provides indication of a transition from the disordered high temperature phase to a lower temperature S1-like S2 structure. The latter resembles LPS 3-like ordering, permeated with an S1-like pattern [c]. An investigation of the energetic hierarchies of these phases supports the hypothesis of the formation of an S1-like S2 structure.

Unfortunately, in the S1-like S2 region, no recent diffraction data are available in order to directly compare experimental with our calculated results, hence we examine SRO data from the region of coherency. In Fig. 15 we show our calculations of the SRO parameters α_{lmn} for 29.8% Pd, where several studies yielded comparable data.

The study above is a characteristic example, how ab-initio based studies can help to clarify uncertain, low-temperature regions in alloy phase diagrams: Contrary to previous

[b] Incoherencies, originating from smoothened APB profiles and wetting around the phase transition cannot be accounted for by our MC simulation, which is restricted to the fcc lattice.

[c] Narrow regions of two-phase coexistence could not be captured by our MC simulation. However, such two-phase regions, even if very narrow, due to Gibbs' phase rule.

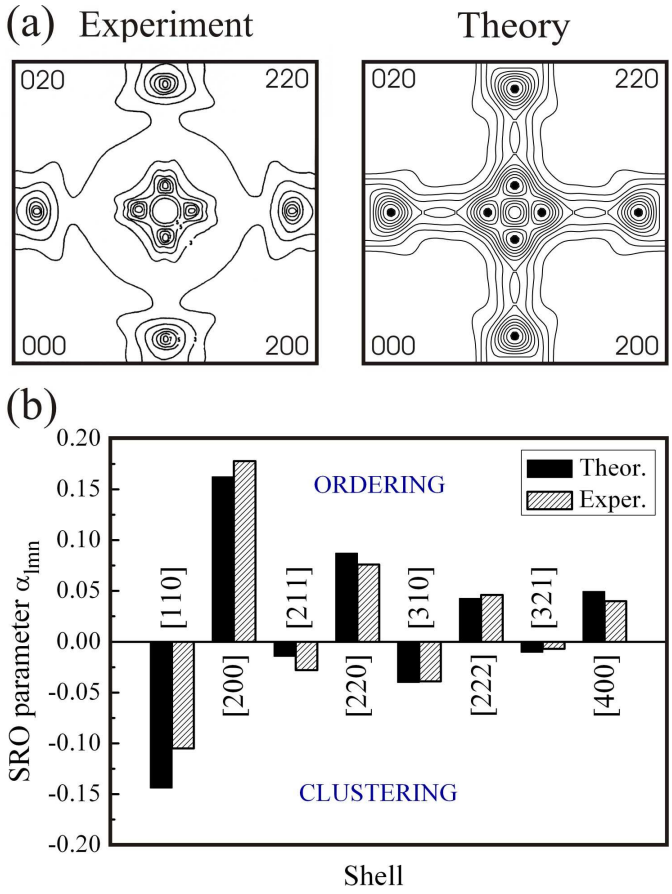

Figure 15. (a) Experimental[81] vs. theoretical short-range order for $Cu_{0.702}Pd_{0.298}$ at T=773 K in reciprocal space. The SRO exhibits peaks of the fundamental wave vector $\mathbf{k} = (1, 1/2M, 0)$ at $M = 3$, in excellent agreement to the superstructure period of S2. (b) Real space SRO for neighboring pairs separated by [hkl].

assessments, Cu-Pd does not have an $L1_2$ ground state, but the Cu_3Pd S2 structure is more stable at 25% composition. Furthermore, a new ground state S1 is predicted at lower composition with Cu_7Pd stoichiometry, hence the features of $L1_2$-like ordering observed experimentally at 17%[78] are due to a S2 with S1-like defects, not due to an $L1_2$ phase.

3.2 Point-defects at grain boundaries

For the Ni-Al system, it is well known that the ordering of defects plays a fundmental role. Understanding the defect structure and stability within the NiAl B2 phase and the Ni_2Al_3 phase is key to understanding the system. In the sense of the cluster expansion lattice, both phases can be described as bcc-based superstructures. It is well known[82–85] that on the simple cubic Ni sublattice of the B2 NiAl phase, vacancies are the dominant defect type in Ni-poor NiAl. Also, if Ni_2Al_3 is to be described as a decoration of Ni and Al atoms on

a bcc lattice, then $\frac{1}{6}$ of the lattice sites are left vacant. Therefore, in order to study defect order with Ni_xAl_{1-x} in the concentration range $0.4 \leq x \leq 0.5$, the cluster expansion needs to explicitly treat vacancies as a third component.

In order to obtain a converged cluster expansion for this system, 129 structures were calculated using VASP. Based on a total number of 711 figures with up to six vertices, the genetic algorithm chose a set of figures with a total of 82 ECI J_F. Two hundred prediction sets, each with $n = 10$ predicted structures, were used to compute the cross-validation-score, resulting in a CV score of $S_{\text{CV}} = 6.0$ meV.

Figure 16 shows the resulting ground state diagram as predicted by UNCLE. The ground state diagram shown in Fig. 16 has been limited to $Ni_xAl_{(1-x)}$ concentrations $0.4 < x < 0.\overline{6}$, as this is the only concentration regime, whithin which bcc-based superstructes are observed experimentally[82,86]. Furthermore this investigation exclusively focused on the description of point defects *within* this concentration regime, which is why the cluster expansion only required convergence for this concentration range. The configuration space search included all ternary bcc-superstructure with 16 sites or less and with less than 21% vacancies. The number of unique configurations is nearly 13 million. To compute these energies of all these configurations using UNCLE requires less than 36 hours on a single 2.8 GHz processor.

Each "□" in Fig. 16 indicates the enthalpy of a structure that was calculated by DFT and included in the cluster expansion to extract the ECIs. Every "+" in the figure corresponds to the cluster expansion prediction for one atomic configuration. Consistent with the observed phase diagram, Ni_2Al_3 and B2 are predicted to be stable at $x = 0.4$ and $x = 0.5$ respectively. The third stable ground state within the converged part of the cluster expansion is Ni_2Al at $x = 0.\overline{6}$, which can be observed experimentally to be a metastable

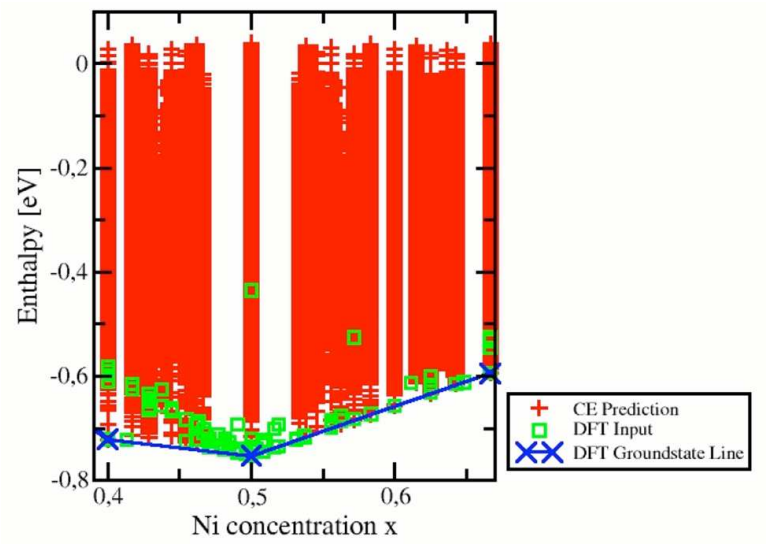

Figure 16. Calculated ground state diagram of all bcc-based superstructures with up to 16 sites occupied by Ni, Al and less than 21% vacancies.

state[86].

The cluster expansion Hamiltonian corresponding to the ground state diagram of Fig. 16 can also be applied to study the defect order at finite temperature. More than the ground state search (which holds no surprises), it is in this context that the cluster expansion is useful for the Ni-Al system. As one example, Fig. 17 provides a view into the ordering of B2-NiAl for $T \approx 4900$K (left) and room temperature (right) resulting from Monte Carlo modelling. The (100) plane shown in the figure is one layer of a Monte Carlo cell consisting of one million lattice sites. The concentration of the three constituents have been fixed to 50% Ni, 45% Al and 5% vacancies.

In full global thermodynamic equilibrium, a Monte-Carlo cell containing 50% of both Ni and Al should exhibit a single B2-ordered domain. Thus a cut along a (100) plane would only contain either Ni- or Al-atoms, depending on whether it lies within the Ni- or the Al-sublattice. Fig. 17 shows that the (100)-plane consists of both Ni- and Al-domains. These regions of Ni and Al belong to different B2-domains, which coexist within the Monte Carlo cell. By changing the external parameters of the simulation, the Monte-Carlo cell can be brought into thermal equilibrium and the different domains visible in Fig. 17 merge into a single B2-domain. While strongly increasing the required calculation time, this does not add any new scientific insight, as the presence of the anti-phase boundaries between different B2 domains does not interfere with the observation of short-ranged vacancy order in the bulk of the respective B2-domains. The important point is to note, that Fig. 17 shows B2-domains with a stacking fault in between them and *not* domains of pure Ni or Al. This allows us to observe Al-subplanes of the B2-structure (light-grey domain) and the Ni-subplanes (dark-grey domains) within a single cut along (100).

For the high temperature case the formation of different B2-domains (dark and light gray) on the lattice can already be observed. The vacancies (white) occupy nearly random sites within Ni- and Al-subplanes. At room temperature the formation of the different B2-domains is complete and the vacancies form diagonal chains within the Ni-subplanes of

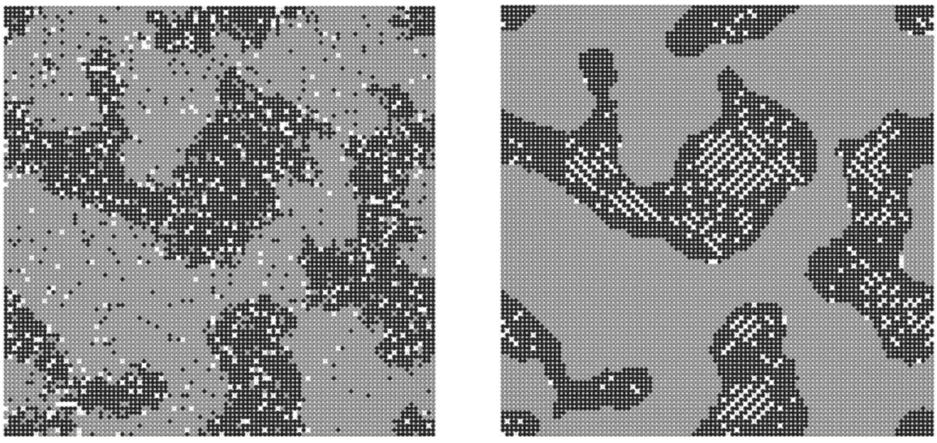

Figure 17. B2-NiAl with 5% vacancies: Cut along the (100) orientation through a $100 \times 100 \times 100$ Monte-Carlo cell for $T = 4936$ K (left) and $T = 294$ K. It can be seen that for lower temperatures all vacancies (white) short range order in the Ni-domains (black).

the B2-phase only. These chains can be interpreted a starting growth of the Ni_2Al_3 phase, where the vacancies are ordered in the same way. Thereby such simulations allow for a quantitative analysis of the phase stability of these alloy phases. A detailed interpretation and evaluation of the structural properties can be found in reference[87].

3.3 Surface Segregation

As known from experimental studies on $Pt_{25}Rh_{75}(111)$[88,89], this surface possesses a characteristic segregation profile: While the top layer shows a Pt enrichment, Pt depletion is found for the layer underneath. The existence of an equilibrium segregation profile is manifested by chemically resolved STM images[88], Low Energy Ion Scattering (LEIS) and quantitative Low Enery Electron Diffraction (LEED) analyses[89]. These studies unambiguously show that for annealing temperatures above $\sim$ 1000 K the observed segregation profile does not longer depend on the experimentally chosen annealing temperature of the sample.

Considering the energetics of the alloy system Pt-Rh, the pronounced segregation profile appears to be a surprise, because formation enthalpies of intermetallic compounds are all between 0 and about -20 meV/atom, i.e. smaller than kT at room temperature. This is in agreement with the bulk phase diagram of this binary system which does not show any long-range ordered structures in the experimentally accessible temperature regime. Instead, a fcc-based solid solution is stable for all concentrations. As a consequence of this small heterogeneous bonding, all constructed effective cluster interactions J_F for bulk and surface are unusually small, possessing energy values much smaller than 20 meV per atom, and cannot explain the characteristic segregation profile found for the (111) surface. However, there is one relevant deviation between the energetic properties of the bulk and the surface: Due to the symmetry break the onsite energies of individual atomic sites which are defined by J_0 and J_1 in Eq.(11) are different for the near-surface layers compared to the bulk. For only weakly ordering systems as the $Pt_{25}Rh_{75}$(111) surface these onsite energies represent a good measure for the segregation behaviour. Actually, it turns out that the top layer shows a tremendous tendency for an enrichment with Pt atoms reflected by an energy gain of about 0.2 eV per atom! Interestingly the opposite is true for the layer underneath: Here, the onsite energy speaks for a Pt depletion and clustering of Rh atoms.

In order to predict the segregation profile quantitatively, Monte-Carlo simulations were performed. As displayed in Fig. 18(left) our constructed cluster expansion is able to reproduce the experimental segregation profile determined via quantitative LEED analysis[89]. It turns out that for this surface system already a 40×40 atom cell per layer was sufficient for a quantitative description of the segregation profile as well as the substitutional ordering. For the latter, fig. 18(right) compares an STM image with atomic and chemical resolution[88] with our predicited one. It can be seen that there is an excellent (quantitative) agreement between experiment and theory.

4 Concluding Remarks

With the program package UNCLE, we present a tool that makes the cluster expansion more accessible to non-specialists and applicable to a wide variety of physical problems. Several extensions of the formalism were presented: Use of the g-representation simplifies

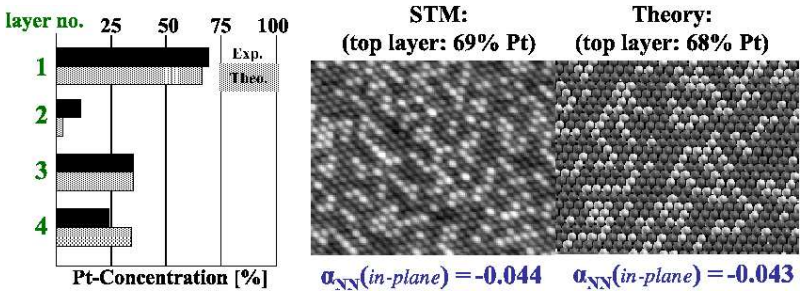

Figure 18. Left: Experimentally determined and predicted segregation profile for $Pt_{25}Rh_{75}(100)$ ($T_{anneal} = 1400$K). Right: Corresponding short range-order behaviour as found by STM and predicted by our CE approach.

and automates the "chores" of setting up and constructing a cluster expansion, performing ground state searches, and using the ECIs in Monte Carlo simulations. By automating much of the cluster expansion construction and use, problems arising from user errors are less likely, resulting in more robust predictions. The treatment of surface alloys and related systems is made possible through the separation of the cluster expansion Hamiltonian into a bulk and surface part.

Since the approach used is only a few years old, its application potential is by no means already reached. There are a number of solid properties which may be treated via DFT, CE, and MC after some further development, as e.g. nucleation processes or cluster from the gas phase. Since the approach allows to describe the behaviour of real alloy systems, a strong interplay with experimental groups is highly desirable.

Acknowledgments

The author gratefully acknowledges support by DFG, MU 1648/2 and Mu 1648/3 (Germany), Studienstiftung des deutschen Volkes, and by the NSF, DMR 0650406.

References

1. P. Villars and L. D. Calvert, *Pearson's Handbook of Crystallographic Data*, ASM International, Materials Park, 1991.
2. L. Reinhard, B. Schönfeld, G. Kostorz, and W. Bührer, Phys. Rev. B, **41**, 1727, 1990.
3. S. Müller and A. Zunger, Phys. Rev. B **63**, 094294, 2001.
4. R. Hultgren, P. D. Desai, D. T. Hawkins, M. Gleiser, K. K. Kelley, *Selected Values of the Thermodynamic Properties of Binary Alloys*, American Society for Metals, Ohio, 1973.
5. J. M. Ziman, *Models of Disorder*, Cambridge University Press, Cambridge, 1979.
6. T. Muto and Y. Tagaki, *Solid State Physics*, vol. 1, p. 193, Academic Press, 1955.
7. L. Guttman, *Solid State Physics*, vol. 3, p. 145, Academic Press, 1956.
8. J. M. Cowley, J. Appl. Phys., **21**, 24, 1950.
9. M. A. Krivoglaz, *X-Ray and Neutron Diffraction in Nonideal Crystals*, Springer, Berlin, 1996.

10. C. J. Sparks and B. Borie, “Local arrangements studied bx x-ray diffraction”, 1966, Met. Soc. Conf.
11. B. Schönfeld, Prog. Mat. Sci., **44**, 435, 1999.
12. P. Hohenberg and W. Kohn, Phys. Rev. **136**, 864B, 1964.
13. W. Kohn and L. J. Sham, Phys. Rev. **140**, 1133A, 1965.
14. J. M. Sanchez, F. Ducastelle, and D. Gratias, Physica A, **128**, 334, 1984.
15. M. C. Payne, M. P. Teter, D. C. Allen, T. A. Arias, J. D. Joannopoulos, Rev. Mod. Phys. **64**, 1064, 1992.
16. R. O. Jones and O. Gunnarsson, Rev. Mod. Phys. **61**, 689, 1989.
17. R. M. Dreizler, E. K. U. Gross, *Density Functional Theory*, Springer, Berlin, 1990.
18. R. M. Dreizler and J. da Providencia, *Density Functional Theory*, Plenum-Press, New York, 1985.
19. E. S. Krachko and E. V. Ludena, *Energy Density Functional Theory of Many electron Systems*, Kluwer Academic, Boston, 1990.
20. D. M. Ceperley and B. J. Alder, Phys. Rev. Lett. **45**, 567, 1980.
21. J. P. Perdew and A. Zunger, Phys. Rev. B **23**, 5048, 1981.
22. J. P. Perdew and Y. Wang, Phys. Rev. B **45**, 13244, 1992.
23. D. J. Singh, *Planewaves, Pseudopotentials and the LAPW Method*, Kluwer, Boston, 1994.
24. D. R. Hamann, M. Schlüter, and C. Chiang, Phys. Rev. Lett. **43**, 1494, 1979.
25. N. Troullier and J. L. Martins, Phys. Rev. B **43** 1993, 1991.
26. D. Vanderbilt, Phys. Rev. B **41**, 7892, 1990.
27. G. Kresse and J. Hafner, J. Phys.: Condens. Matter, **6**, 8245, 1994.
28. G. Kresse and D. Joubert, Phys. Rev. B, **59**, no. 3, 1758–1775, Jan 1999.
29. P. E. Blöchl, Phys. Rev. B **50**, 17953, 1994.
30. A. Zunger, in: Handbook of Crystal Growth, T.D.J. Hurle, (Ed.), vol. 63, p. 99, Elsevier, Amsterdam. 1994, and references therein.
31. D. M. Wood and A. Zunger, Phys. Rev. Lett., **61**, 1501, 1988.
32. V. Ozoliņš, C. Wolverton, and A. Zunger, Phys. Rev. B, **57**, 4816, 1998.
33. V. Ozoliņš, C. Wolverton, and A. Zunger, Phys. Rev. B, **57**, 6427, 1998.
34. D. J. Bottomeley and P. Fons, J. Cryst. Growth, **44**, 513, 1978.
35. D. B. Laks, L. G. Ferreira, S. Froyen, and A. Zunger, Phys. Rev. B, **46**, 12587, 1992.
36. A. Zunger, in: NATO ASI on: Statics and Dynamics of Alloy Phase Transformations, P. E. A. Turchi and A. Gonis, (Eds.), p. 361, Plenum Press, New York. 1994.
37. D. Lerch, O. Wieckhorst, G. L. W. Hart, R. W. Forcade, and S. Müller, submitted to Modelling Simul. Mater. Sci. Eng.
38. Georg Kresse and Jürgen Hafner, Phys. Rev. B, **47**, 558, 1993.
39. Georg Kresse and J. Furthmüller, Phys. Rev. B, **54**, 11169, 1996.
40. Georg Kresse and J. Furthmüller, Comp. Mat. Sci, **6**, 15, 1996.
41. E. Wimmer, H. Krakauer, M. Weinert, and A. J. Freeman, Phys. Rev. B, **24**, no. 2, 864–875, Jul 1981.
42. M. Weinert, J. Math. Phys., **22**, no. 11, 2433, Nov 1981.
43. M. Weinert, E. Wimmer, and A. J. Freeman, Phys. Rev. B, **26**, no. 8, 4571–4578, Oct 1982.
44. L. G. Ferreira, S.-H. Wei, and A. Zunger, J. Supercomp. Appl., **5**, 34, 1991.
45. S. Müller, J. Phys.: Cond. Matter, **15**, 2003.

46. Gus L. W. Hart and Rodney W. Forcade, Phys. Rev. B, **77**, no. 22, 224115, 2008.
47. C. Wolverton and D. de Fontaine, Phys. Rev. B, **49**, no. 13, 8627, 1994.
48. Volker Blum, Gus L. W. Hart, Michael J. Walorski, and Alex Zunger, Phys. Rev. B, **72**, no. 16, 165113, 2005.
49. G. L. W. Hart, V. Blum, J. Walorski, and A. Zunger, Nature Materials, **4**, no. 5, 391, 2005.
50. A. van de Walle and G. Ceder, Journal of Phase Equilibria, **23**, 348, 2002.
51. K. Baumann, Trends in Analytical Chemistry, **22**, 395, 2003.
52. S. Müller, M. Stöhr, and O. Wieckhorst, Applied Physics A, **82**, no. 3, 415, 2005.
53. Nikolai A. Zarkevich and D. D. Johnson, Phys. Rev. Lett., **92**, no. 25, 255702, Jun 2004.
54. Alejandro Diaz-Ortiz and Helmut Dosch, Phys. Rev. B, **76**, no. 1, 012202, 2007.
55. Alejandro Díaz-Ortiz, Helmut Dosch, and Ralf Drautz, Journal of Physics: Condensed Matter, **19**, no. 40, 406206, 2007.
56. J. W. D. Conolly and A. R. Williams, Phys. Rev. B, **27**, 5169, 1983.
57. G. D. Garbulsky and G. Ceder, Phys. Rev. B, **49**, no. 9, 6327–6330, Mar 1994.
58. D. Goldfarb and A. Idnani, Math. Prog., **27**, 1, 1983.
59. R. Drautz, H. Reichert, M. Fähnle, H. Dosch, and J. M. Sanchez, Phys. Rev. Lett., **87**, no. 23, 236102, Nov 2001.
60. S. Müller, Surface and Interface Analysis, **38**, 1158, 2006.
61. T. Kerscher, O. Wieckhorst, and S. Müller, to be submitted.
62. C. Wolverton, V. Ozoliņš, and A. Zunger, J. Phys.: Condens. Matter, **12**, 2749, 2000.
63. N. Metropolis, A. W. Rosenbluth, M. V. Rosenbluth, A. Teller, and E. Teller, J. Chem Phys., **60**, 1071, 1974.
64. M. Toda, R. Rubo, and N. Saito, *Statistical Physics I*, Springer, Berlin, 1983.
65. S. Müller, L.-W. Wang, A. Zunger, and C. Wolverton, Phys. Rev. B, **60**, 16448, 1999.
66. J. L. Murray, Int. Met. Rev., **30**, 211, 1985.
67. J. Jacobsen, K. W. Jacobsen, and P. Stoltze and. J. K. Norskov, Phys. Rev. Lett., **74**, 2295, 1995.
68. A. B. Börtz, M. H. Kalos, and J. L. Lebowitz, J. Comp. Phys., **17**, 10, 1975.
69. S. Müller, L.-W. Wang, and A. Zunger A., Model. Simul. Mater. Sci. Eng., **10**, 131, 2002.
70. S. Müller, C. Wolverton, L.-W. Wang, and A. Zunger, Acta Mater. **48**, 4007, 2000.
71. Z. W. Lu, D. B. Laks, S. H. Wei, and A. Zunger, Phys. Rev. B, **50**, 6642, 1994.
72. S. Bärthlein, G. L. W. Hart, A. Zunger, and S. Müller, J. Phys.: Condens. Matter **19**, 032201, 2007.
73. S. Bärthlein, E. Winning, G. L. W. Hart, and S. Müller, Acta Mater., in press.
74. G. Ceder, D. de Fontaine, H. Dreysse, D. M. Nicholson, G. M. Stocks, and Gyorffy B. L., Acta metall. mater., **38**, 2299, 1990.
75. A. V. Ruban, S. Shallcross, S. I. Simak, and H. L. Skriver, Phys. Rev. B, **70**, 125115, 2004.
76. C. Colinet and A. Pasturel, Phil. Mag. B, **82**, 1067, 2002.
77. Z. W. Lu, S.-H. Wei, Alex Zunger, S. Frota-Pessoa, and L. G. Ferreira, Phys. Rev. B, **44**, no. 2, 512–544, Jul 1991.
78. D. Broddin, G. Van Tendeloo, J. Van Landuyt, S. Amelinckx, R. Portier, M. Guymont, and A. Loiseau, Phil. Mag. A, **54**, 395, 1986.

79. S. Takeda, J. Kulik, and D. de Fontaine, Acta metall., **35**, 2243, 1987.
80. S. Takeda, J. Kulik, and D. de Fontaine, J. Phys. F, **18**, 1387, 1988.
81. Kenichi Oshima and Denjiro Watanabe, Acta Cryst. A, **32**, 883, 1976.
82. A. Taylor and N. J. Doyle, Journal of Applied Crystallography, **5**, no. 3, 201–209, Jun 1972.
83. C. L. Fu, Y.-Y. Ye, M. H. Yoo, and K. M. Ho, Phys. Rev. B, **48**, no. 9, 6712–6715, Sep 1993.
84. B. Meyer and M. Fähnle, Phys. Rev. B, **59**, no. 9, 6072–6082, Mar 1999.
85. F. Lechermann and M. Fähnle, Phys. Rev. B, **63**, no. 1, 012104, Dec 2000.
86. F. Reyaud, Journal of Applied Crystallography, **9**, no. 4, 263–268, Aug 1976.
87. D. Lerch and S. Müller, to be submitted.
88. E.L.D. Hebenstreit, M. Hebenstreit, M. Schmid, and P. Varga, Surface Science, **441**, 441, 1999.
89. E. Platzgummer, M. Sporn, R. Koller, S. Forsthuber, M. Schmid, W. Hofer, and P. Varga, Surface Science, p. 236, 1999.